16

Giant Moment Enhancement of Magnetic Nanoparticles Embedded in Multi-Walled Carbon Nanotubes: Consistent with Ultrahigh Temperature Superconductivity

Guo-meng Zhao[1,2], Jun Wang[2], Yang Ren[3] and Pieder Beeli[1]

[1] *Department of Physics and Astronomy, California State University at Los Angeles, Los Angeles*

[2]*Department of Physics, Faculty of Science, Ningbo University, Ningbo*

[3]*X-Ray Science Division, Advance Photon Source, Argonne National Laboratory, Argonne*

[1,3,4]*USA*

[1,2]*P. R. China*

1. Introduction

There are reports of intrinsic weak ferromagnetism in graphite and carbon-based materials well above room temperature Cervenka et al. (2009); Esquinazi et al. (2003); Kopelevich et al. (2000); Mendoza et al. (1999); Moehlecke et al. (2002); Mombru et al. (2005), as well as a theoretical prediction of a ferromagnetic instability in graphene sheets Bas & Jafari (2002). On the other hand, Dzwilewski *et al.* Talyzin et al. (2007) show that the observed high-temperature ferromagnetism in rhombohedral C_{60} Makarova et al. (2001) is not intrinsic but caused by contamination of magnetic impurities. In addition to the observation of unusual high-temperature ferromagnetism in the carbon-based materials, there was a report of extra magnetic moment induced in graphite due to a large magnetic proximity effect between graphite and magnetic nanoparticles Coey et al. (2002). Similarly, high-temperature magnetic data of multi-walled carbon nanotube (MWCNT) mat samples embedded with Fe and Fe_3O_4 nanoparticles Zhao et al. (2008) indicated that the room-temperature saturation magnetizations of the magnetic nanoparticles embedded in the MWCNTs are enhanced by a factor of about 3 as compared with what they would be expected to have for free magnetic nanoparticles. Recently, the study has been extended to nickel nanoparticles embedded in MWCNTs Wang et al. (2010) and shown a similar enhancement factor.

More intriguringly, there were reports of ultrahigh temperature superconducting behaviors in carbon films Antonowicz (1974); Lebedev (2004), carbon nanotubes Zhao & Wang (2001); Zhao (2004; 2006), graphite Kopelevich et al. (2000), and graphite-sulfur composites Da Silva et al. (2001); Moehlecke et al (2004). Highly oriented pyrolithic graphite (HOPG) was shown to display either a partial superconducting or a ferromagnetic-like response to an applied magnetic field up to 400 K Kopelevich et al. (2000).

The existence of ultrahigh temperature superconductivity in the carbon-based materials is not accidental. The unique electronic structures of the carbon-based materials make them

ideal for high-temperature superconductivity. Several theoretical models based on different types of interactions predict high-temperature superconductivity in quasi-one-dimensional (quasi-1D) and/or quasi-two-dimensional (quasi-2D) electronic systems. Alexandrov and Mott Alexandrov & Mott (1995) demonstrated that strong electron-phonon coupling can lead to the formation of intersite bipolarons and that the Bose-Einstein condensation of the bipolarons can explain high-temperature superconductivity in cuprates. Little Little (1964) proposed that high-temperature or room-temperature superconductivity could be realized by exchanging high-energy excitons in quasi-1D systems. Lee and Mendoza showed that superconductivity as high as 500 K can be achieved through a pairing interaction mediated by undamped acoustic plasmon modes in quasi-1D systems Lee & Mendoza (1989). High-temperature superconductivity can also occur in a multi-layer electronic system due to an attraction of charge carriers in the same conducting layer via exchange of virtual plasmons in neighboring layers Cui & Tsai (1991). If the plasmon-mediated pairing mechanisms are relevant, one should be able to find high-temperature superconductivity in quasi-one-dimensional and/or multi-layer systems such as cuprates, carbon nanotubes (CNTs), and graphites. In contrast to the mechanisms based on the attractive interactions between electrons by virtually exchanging phonons, excitons, and/or plasmons, an exotic model based on resonating-valence-bond (RVB) theory originally proposed by Anderson Anderson (1987) even predicts ultrahigh temperature *d*-wave superconductivity in heavily doped graphene Black-Schaffer & Doniach (2007). Gonzalez *et al.* Gonzalez et al. (2001) showed that both high-temperature ferromagnetic and *p*-wave superconducting instabilities can occur in defective regions of graphite, where topological disorder enhances the density of states. Schrieffer Schrieffer (2004) predicted ultrahigh temperature superconductivity at a quantum critical point where ferromagnetic fluctuations are the strongest.

In this article, we will present the detailed magnetic properties of multi-walled carbon nanotubes embedded with Ni Wang et al. (2010), Fe Zhao et al. (2008; 2011), Fe_3O_4 Zhao et al. (2008; 2011), and Fe_3C magnetic nanoparticles. Magnetic measurements were carried out using Quantum Design vibrating sample magnetometer (VSM). Inductively coupled plasma mass spectrometer and high energy synchrotron x-ray diffractometer were used to accurately determine the impurity concentrations. Scanning electron microscope and/or transmission electron microscopy were used to characterize MWCNTs and magnetic nanoparticles embedded. In sections 2,3, and 4, we will present the detailed experimental results for multi-walled carbon nanotubes embedded with Fe_3C, Ni, Fe, and Fe_3O_4 magnetic nanoparticles. We found that the saturation magnetizations of Fe, Fe_3O_4, and Ni magnetic nanoparticles are enhanced by a factor of about 3 as compared with what they would be expected to have for free magnetic nanoparticles. In contrast, a smaller enhancement factor (1.6) is found for Fe_3C nanoparticles. In section 5, we will provide possible theoretical interpretations to the giant moment enhancements. The results cannot be explained by a magnetic-proximity model but can be naturally explained in terms of ultrahigh temperature superconductivity in MWCNTs. In section 6, we will identify the diamagnetic Meissner effect in the magnetic field parallel to the tube axis up to room temperature for aligned MWCNTs that are physically separated and have negligibly small magnetic impurities. The magnitude of the Meissner effect is in quantitative agreement with the predicted penetration depth expected from the measured carrier density. In section 7, we will give concluding remarks and discuss possible microscopic mechanisms for high-temperature superconductivity in carbon nanotubes.

2. Magnetic properties of Fe_3C nanoparticles embedded in MWCNTs

Purified MWCNT mat samples (Catalog No. PD15L520) from Nanolab were synthesized by chemical vapor deposition under catalyzation of Fe nanoparticles. The average outer diameter is about 15 nm and the average inner diameter is about 10 nm. The morphology of the mat sample can be seen from scanning electron microscopy (SEM) image shown in Fig. 1a. The SEM image was taken by a field emission scanning electron microcopy (FE-SEM, Hitachi S-4800) using an accelerating voltage of 2 kV. One can see that the outer diameters of these MWCNTs are in the range of 10-20 nm and centered around 15 nm, in agreement with the product specification from Nanolab. Fig. 1b shows a transmission electron microscopic (TEM) image of the mat sample, which was provided by Nanolab. The image reveals the multiwall nature of the carbon nanotubes with a mean inner diameter of about 10 nm.

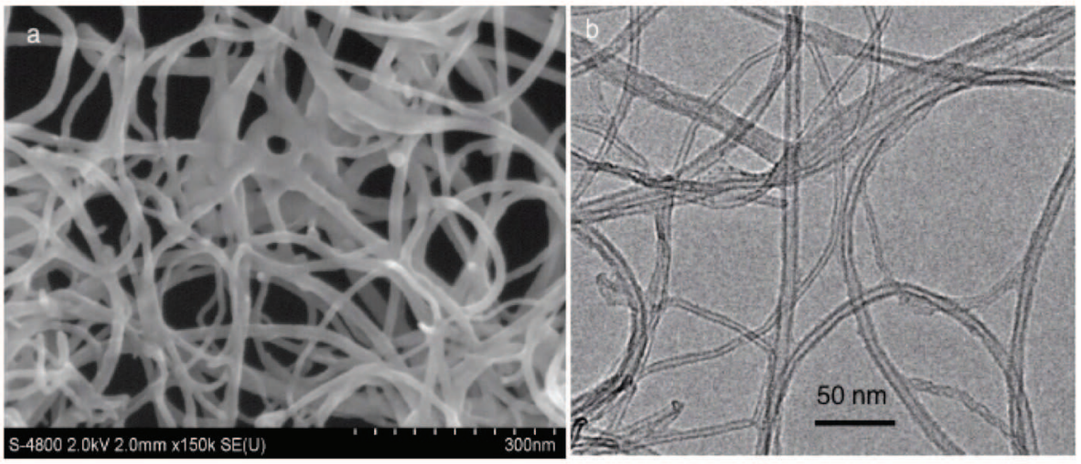

Fig. 1. a) SEM image of a MWCNT mat sample of PD15L520. b) TEM image of the MWCNT mat sample.

The total metal-based impurity concentrations of the mat sample can be determined from the composition analysis of the residual of the sample, which was obtained by burning off carbon-based materials in air. A Perkin-Elmer Elan-DRCe inductively coupled plasma mass spectrometer (ICP-MS) was used to analyze the composition of the residual. From the weight (3.6%) of the residual and the ICP-MS analysis, we obtain the metal-based magnetic impurity concentrations in weight: Ni = 0.01936%, Fe = 1.001%, and Co = 0.00102%. The Fe concentration determined from our ICP-MS is in excellent agreement with the product specification (Fe = 0.94%) from Nanolab.

Since the magnetic impurity phases are so minor, it is impossible to identify the minor phases from a normal low-energy x-ray diffraction (XRD) spectrum. But we can achieve this goal by performing high-energy synchrotron x-ray diffraction experiment. Fig. 2 shows synchrotron XRD spectrum for the mat sample along with the standard spectrum of Fe_3C. The XRD spectrum was taken on a high-energy synchrotron x-ray beam-line 11-ID-C at the Advanced Photon Source, Argonne National Laboratory, using monochromatic radiation with a wavelength of $\lambda = 0.1078$ Å. The major peaks in the spectrum of Fig. 2 correspond to the diffraction peaks of the MWCNTs Reznik et al. (1995) and Fe_3C. In particular, the (002) diffraction peak of the MWCNTs is seen at $2\theta = 1.786^\circ$.

Figure 3a shows XRD intensity as a function of the wave-vector transfer Q for the (002) peak of a pure MWCNT sample. The data are digitized from Reznik et al. (1995). The solid red

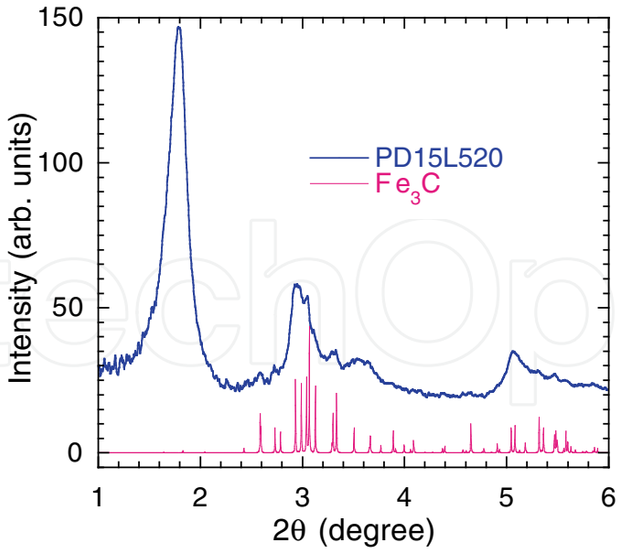

Fig. 2. High-energy synchrotron x-ray diffraction (XRD) spectrum for a virgin MWCNT sample of PD15L520 and the standard spectrum of Fe_3C.

line in Fig. 3a is the fitted curve by the sum of a Gaussian and a cut-off Lorentzian function, which takes into account both domain size broadening and strain broadening Reznik et al. (1995). The Lorentzian function is cut off to zero when $|Q - Q_\circ| \geq 3.65\gamma$, where $Q_\circ$ is the peak position and γ is the full width at half maximum (FWHM). The integrated intensity of the cut-off Lorentzian is 91.4% of the intensity of the corresponding full Lorentzian. In Fig. 3b, we display the expanded view of the (002) peak of our mat sample. We also fit the data with the sum of a Gaussian and a cut-off Lorentzian function (solid red line). It is apparent that the fit is excellent. In Fig. 3c and Fig 3d, we show the expanded views at 2θ around 2.6° and 3.3°, respectively. At 2θ around 2.6°, there are closely spaced double peaks, corresponding to the (121) and (210) diffraction peaks of the Fe_3C phase. The intensity of the (121) peak is higher than that of the (210) peak by a factor 1.52. The solid red line in Fig. 3c is the best fitted curve by the sum of two Gaussian functions with the intensity ratio of 1.52 and peak separation of 0.008°, which are consistent with the standard spectrum of the Fe_3C phase. The Gaussian function is consistent with particle-size broadening Reznik et al. (1995). From the best fit, we obtain γ = 0.0589° for both peaks. The integrated intensity of the two Gaussian peaks is calculated to be 0.501±0.035% of the intensity of the MWCNT (002) peak. Using the standard intensities of graphite's (002) peak and Fe_3C's (121) and (210) peaks and assuming that the intensity of MWCNT (002) peak is the same as that of graphite (002) peak, we find that the Fe_3C concentration is 0.935±0.065% (in weight). This corresponds to the Fe concentration of 0.874±0.061%, which is in good agreement the total Fe concentration (1.00%) determined from the ICP-MS above and also close to the product specification for the Fe concentration (0.94%). This implies that the dominant Fe-based phase is Fe_3C and the minor phases may also contain Fe and/or Fe oxides, which are not visible from the XRD spectrum.

Similarly, at 2θ around 3.3°, there are also closely spaced double peaks, corresponding to the (131) and (221) diffraction peaks of the FeC_3 phase. The intensity for the (131) peak is 2/3 of that for the (221) peak. The solid red line in Fig. 3d is the best fitted curve by the sum of two Gaussian functions with the intensity ratio of 2/3 and peak separation of 0.038°. The peak widths are kept the same as those of the (121) and (210) peaks. The integrated intensity of the double Gaussian peaks is calculated to be 0.811±0.024% of the intensity of the MWCNT (002)

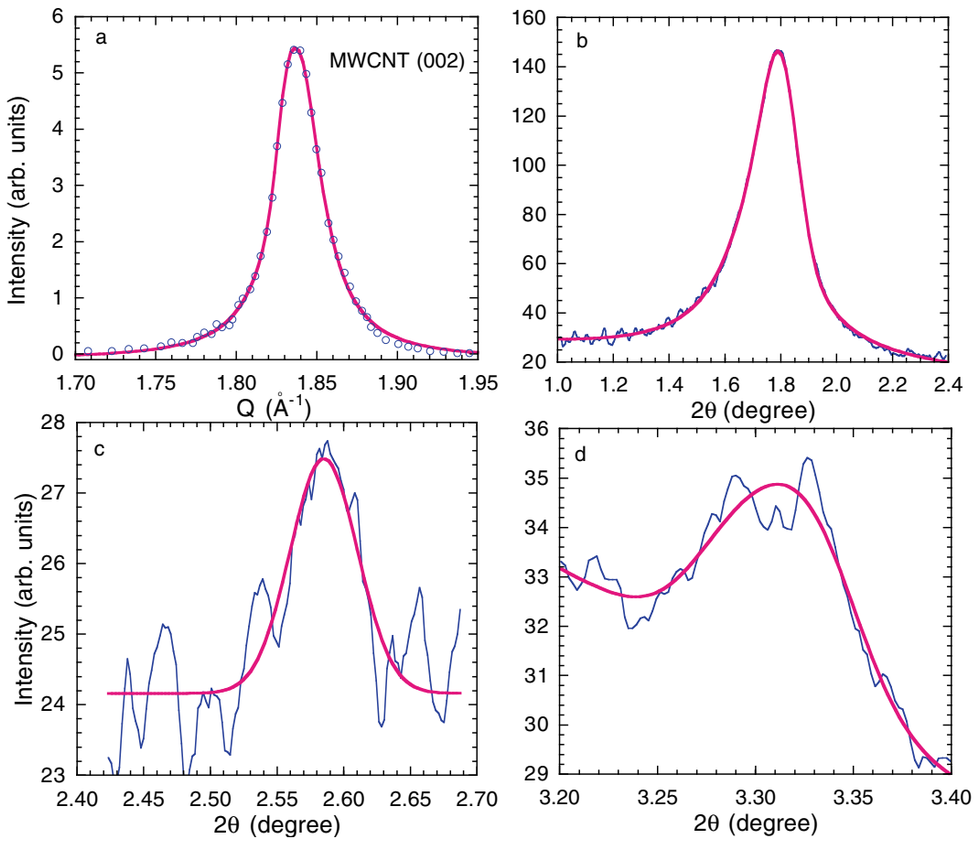

Fig. 3. a) The XRD intensity as a function of the wave-vector transfer Q for the (002) peak of a pure MWCNT sample. The data are digitized from Reznik et al. (1995). b) The expanded view of the MWCNT (002) peak of sample PD15L520. c) The expanded view at 2θ around 2.6° of sample PD15L520. There are closely spaced double peaks, corresponding to the (121) and (210) diffraction peaks of the Fe_3C phase. d) The expanded view at 2θ around 3.3°. There are also closely spaced double peaks, corresponding to the (131) and (221) diffraction peaks of the FeC_3 phase.

peak. The intensity ratio implies that the Fe_3C concentration is 0.947±0.028% (in weight), in excellent agreement with that (0.935±0.065%) inferred from the (121) and (210) peaks above. It is important to determine the average diameter d of the ferromagnetic Fe_3C nanoparticles embedded in MWCNTs. We can determine d from the peak width of the XRD spectrum. The full width at half maximum has been found to be 0.0589°. Using the Scherrer equation: $d = 0.89\lambda/(\gamma_b \cos\theta)$ and the width $\gamma_b = 0.0546°$ (after correcting for the instrumental broadening), we calculate d = 10.0 nm, in good agreement with the average inner diameter of the tubes (see Fig. 1b).

Fig. 4a shows magnetization versus magnetic field for the MWCNT mat sample at 310 K. The magnetization was measured using a Quantum Design vibrating sample magnetometer. The linear field dependence of the magnetization with a negative slope at $H > 20$ kOe is due to the diamagnetic contribution. The linear extrapolation to $H = 0$ yields $M_s = 1.53$ emu/g. In Fig. 4b, we present temperature dependence of the saturation magnetization M_s for the mat sample. It is clear that the M_s value is small (0.05 emu/g) above the Curie temperature (about 470 K) of the Fe_3C phase. Therefore, the saturation magnetization for the Fe_3C phase is 1.47 emu/g.

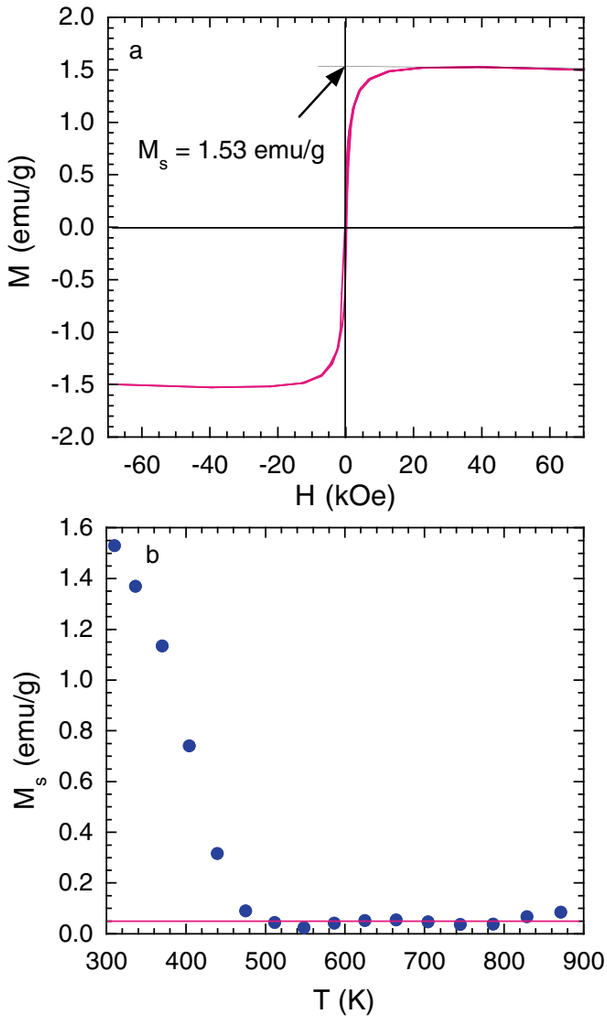

Fig. 4. a) The magnetization versus magnetic field for sample PD15L520 at 310 K. b) The temperature dependence of the saturation magnetization M_s for the mat sample.

With the Fe_3C concentration of 0.94±0.07%, we calculate the saturation magnetization to be 156±11 emu per gram of Fe_3C.

For 11-nm Fe_3C nanoparticles embedded in carbon matrix and prepared at 900 °C, M_s was found to be 89-97 emu per gram of Fe_3C and the reduced remanence is 0.16-25 [see Sajitha et al. (2007)]. The reduced remanence in our 10-nm Fe_3C nanoparticles embedded in MWCNTs is about 0.18, very close to those of the samples prepared at 900 °C. Therefore, M_s of our 10-nm Fe_3C nanoparticles embedded in MWCNTs is enhanced by a factor of 1.6±0.2, compared with that (93±4 emu/g) of free Fe_3C particles. This enhancement factor is significantly lower than those for Ni, Fe, and Fe_3O_4 nanoparticles (see below). It is interesting to note that sample CFe05980 of Sajitha et al. (2007), prepared at 980 °C, has a large M_s value of 169 emu per gram of Fe_3C. These authors tentatively attributed this large value to the proximity of the nanoparticles to carbon nanotubes, which may have been formed at this higher temperature. Our current results support this interpretation.

3. Magnetic properties of nickel nanoparticles embedded in MWCNTs

MWCNT mat samples embedded with nickel nanoparticles were obtained from SES Research of Houston (Catalog No. TS0636). The mat samples were synthesized by chemical vapor deposition under catalyzation of nickel nanoparticles. The morphology of the mat sample can be seen from scanning electron microscopy images shown in Fig. 5a and Fig. 5b. One can see that the mean outer diameter of these MWCNTs is around 35 nm. The mean inner diameter of the MWCNTs is about 15±5 nm, as seen from the transmission electron microscopy image (Fig. 5c) recorded by FEI Tecnai F20 with an accelerating voltage of 200 kV. The nickel nanoparticles sit inside the innermost shells near the ends of the tubes, as labeled by A, B, C, and D in Fig. 5d. Some nickel nanoparticles are connected to form a continuous chain (see a location labeled by D in Fig. 5d).

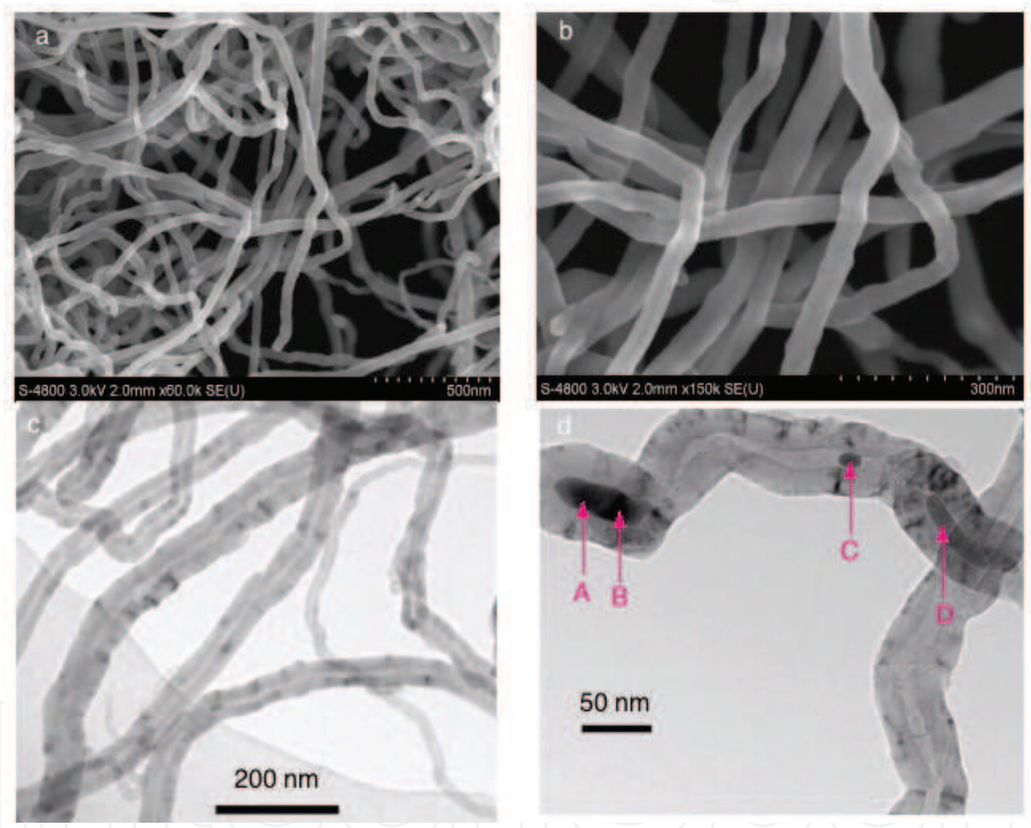

Fig. 5. a) SEM image of a MWCNT mat sample of TS0636. b) SEM image of the MWCNT mat sample with a higher magnification. c) TEM image of the MWCNT mat sample. c) TEM image of a selected MWCNT filled with nickel nanoparticles labeled by A, B, C, and D. After Wang et al. (2010).

The metal-based impurity concentrations of the mat sample were also determined from ICP-MS, which yielded the metal-based magnetic impurity concentrations in weight: Ni = 0.476%, Fe = 0.00907%, and Co = 0.0133%. The major impurity phase is nickel, in agreement with the sample preparation condition.

We also determined the concentration of the ferromagnetic phase of nickel from the high-energy synchrotron x-ray diffraction spectrum. Fig. 6a shows synchrotron XRD spectrum for a MWCNT sample of TS0636 along with the standard spectrum of the

face-centered cubic (fcc) phase of Ni. The major peaks in the spectrum of Fig. 6a correspond to the diffraction peaks of MWCNTs and the fcc phase of Ni. The Ni (311) peak is clearly seen at $2\theta = 5.815°$.

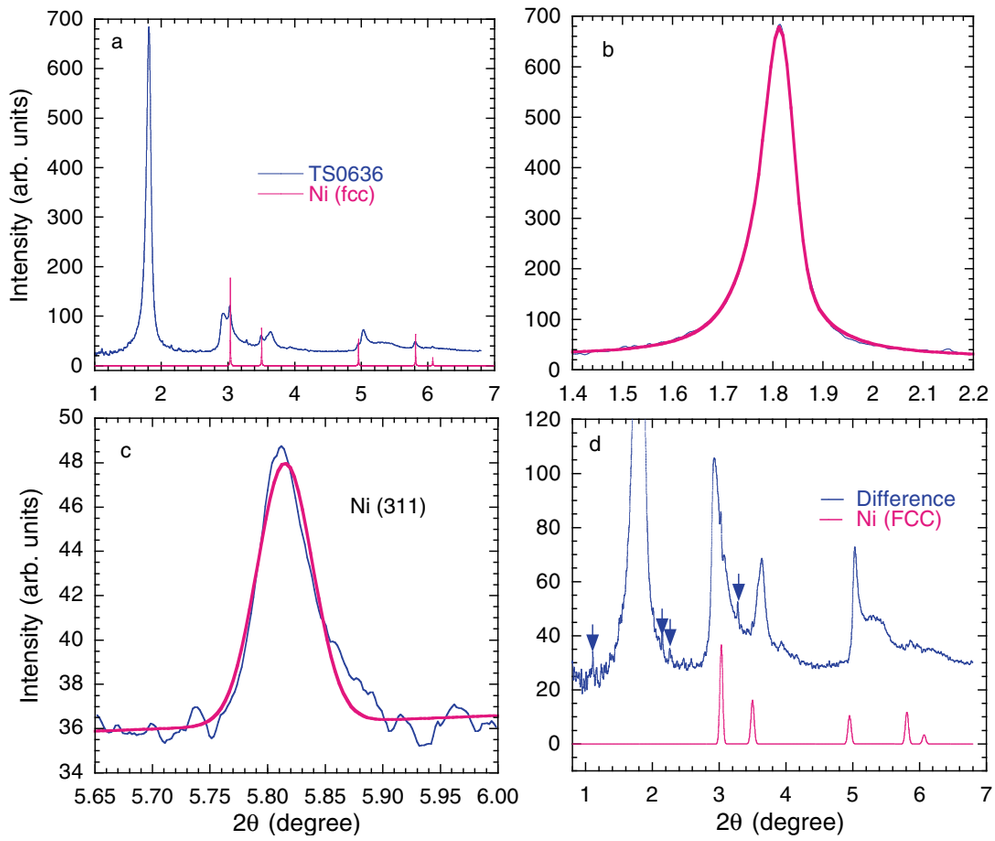

Fig. 6. a) High-energy synchrotron x-ray diffraction spectrum of sample TS0636 along with the standard spectrum of the face-centered cubic (fcc) phase of Ni. b) The expanded view of of the MWCNT (002) peak. c) The expanded view of of the Ni (311) peak. d) The expected XRD spectrum of the fcc Ni (red line) based on the nickel concentration (0.45%) and the difference spectrum (blue line), which is obtained by subtracting the Ni spectrum from the spectrum of TS0636 in Fig. 6a. After Wang et al. (2010).

Figure 6b and Fig. 6c display the expanded views of the MWCNT (002) and Ni (311) peaks, respectively. The solid red line in Fig. 6b is the fitted curve by the sum of a Gaussian and a cut-off Lorentzian function. The solid red line in Fig. 6c is the fitted curve by a Gaussian function. The integrated intensity of the Ni (311) peak is found to be $0.882\pm0.020\%$ of the intensity of the MWCNT (002) peak. From the intensity ratio, we find that the ferromagnetic fcc nickel concentration is $0.451\pm0.010\%$ (in weight), which is slightly lower than the total Ni concentration (0.476%) inferred from ICP-MS. This implies that the ferromagnetic fcc nickel is the dominant phase while the concentrations of other nonmagnetic nickel-based phases are too small to be seen in the XRD spectrum.

In order to check the reliability of our inferred ferromagnetic nickel concentration based on the Ni (311) peak, we show, in Fig. 6d, the expected XRD spectrum of the fcc Ni with the concentration of 0.451% (lower curve in Fig. 6d) and the difference spectrum (upper curve in Fig. 6d), which is obtained by subtracting the Ni spectrum from the spectrum of sample

TS0636 in Fig. 6a. The difference spectrum shows no observable residual of any peaks of the fcc nickel, implying that the inferred Ni concentration is indeed reliable. Furthermore, all the peaks except for some peaks indicated by arrows in the difference spectrum agree with the peaks observed in pure MWCNTs Reznik et al. (1995). The extra peaks indicated by the arrows should be associated with other impurity phases.
It is also essential to determine the average diameter d of the ferromagnetic Ni nanoparticles embedded in MWCNTs. The full width at half maximum of the Ni (311) peak is found to be 0.0556° from the Gaussian fit in Fig. 6c. Using the Scherrer equation: $d = 0.89\lambda/(\gamma_b \cos\theta)$ and the width γ_b = 0.0511° (after correcting for the instrumental broadening), we calculate d = 11 nm, close to the average inner diameter of the tubes (see Fig. 5c).

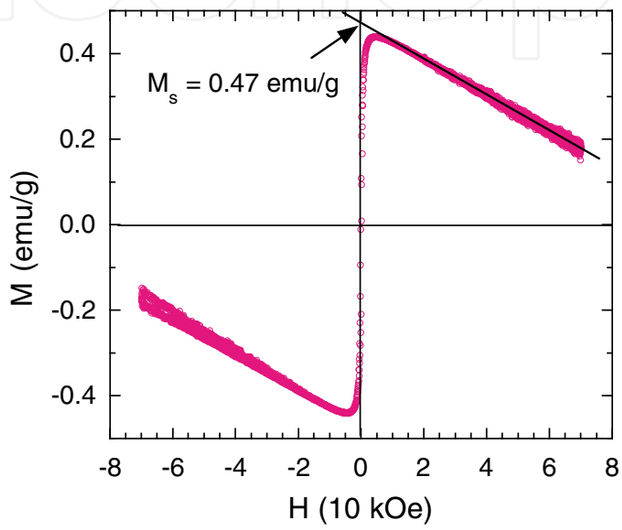

Fig. 7. Magnetic hysteresis loop of sample TS0636 at 320 K. After Wang et al. (2010).

Figure 7 shows magnetization versus magnetic field for the Ni-filled MWCNT mat sample at 320 K. The linear extrapolation to $H = 0$ yields $|\chi_{dia}| = 4.2\times10^{-6}$ emu/g and M_s = 0.47 emu/g. With the ferromagnetic nickel concentration of 0.451% in the Ni-filled MWCNT sample, we calculate the M_s value to be 104 emu per gram of nickel. The saturation magnetization of the 11-nm nickel nanoparticles embedded in MWCNTs is a factor of 3.4 larger than the known M_s = 30-32 emu/g for pure fcc Ni nanoparticles with d = 11-12 nm Chen &Hsieh (2002); Gong et al. (1991). It is also a factor of 1.9 larger than that (55 emu/g) for the bulk nickel. Thus, there is a giant magnetic moment enhancement of the Ni nanoparticles when they are embedded inside the MWCNTs, in contrast to the case for Fe_3C nanoparticles, where the enhancement factor is much smaller.

4. Magnetic properties of Fe and Fe_3O_4 nanoparticles embedded in MWCNTs

MWCNT mat samples embedded with Fe and Fe_3O_4 nanoparticles were obtained from SES Research of Houston (Catalog No. RS0657). The mat samples were synthesized by chemical vapor deposition under catalyzation of Fe nanoparticles. During purification process, some Fe nanoparticles were oxidized into the Fe_3O_4 and α-Fe_2O_3 phases and were removed by HCl. Nevertheless, some fractions of Fe, Fe_3O_4, and α-Fe_2O_3 nanoparticles may still remain inside and/or outside the tubes due to incomplete purification, in agreement with high-energy synchrotron x-ray diffraction data Zhao et al. (2011).

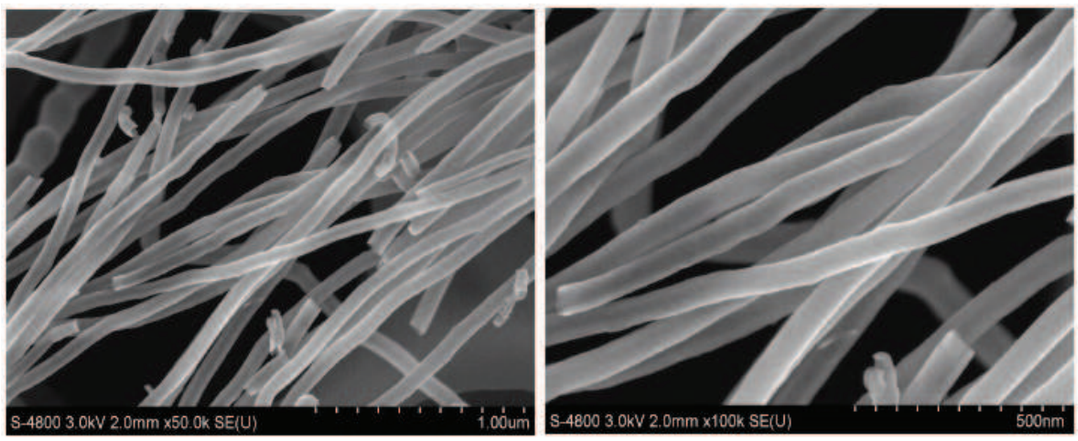

Fig. 8. SEM images of a MWCNT mat sample of RS0637.

The morphology of the mat sample can be seen from scanning electron microscopy images shown in Fig. 8. It is clear that the tubes are quite uniform and the mean outer diameter of these MWCNTs is about 70 nm. The mean inner diameter of the MWCNTs is estimated to be about 50 nm from the mean outer diameter and the mean wall thickness of the MWCNTs (about 10 nm) determined from the width of the XRD (002) peak Zhao et al. (2011).

The total metal-based impurity concentrations of the mat sample were determined from the ICP-MS analysis of the residual of the mat sample (1.73±0.05%), which was obtained by burning off carbon-based materials in air at 550 °C for about 10 minutes. The metal-based magnetic impurity concentrations in weight were found to be: Fe = 0.69±0.02%, Co = 0.0036±0.0001%, and Ni = 0.0021%. The major impurity phase is Fe, in agreement with the sample preparation condition.

Quantitative analyses on the high-energy XRD data Zhao et al. (2011) have shown that the mat sample contains (in weight): Fe = 0.241±0.004%; α-Fe_2O_3 = 0.216±0.015%, and Fe_3O_4 = 0.250±0.010%. The Fe concentration contributed from the α-Fe, α-Fe_2O_3, and Fe_3O_4 phases is calculated to be 0.58±0.02%, which is about 0.11±0.04% lower than the total Fe concentration (0.69±0.02%) determined from the ICP-MS. The mean diameters of Fe, α-Fe_2O_3, and Fe_3O_4 nanoparticles are 46 nm, 23 nm, and 18 nm, respectively.

The total Fe concentration determined from the ICP-MS is also in quantitative agreement with the magnetization data of the residual where α-Fe_2O_3 is the only possible Fe-based phase. We have shown Wang et al. (2011) that α-Fe_2O_3 nanoparticles can be completely reduced to the magnetic Fe_3O_4 phase after the sample was heated up to 1000 K during the magnetic measurement (due to a high vacuum environment inside the VSM system). In Fig. 9a, we plot the high-field (10 kOe) magnetization versus temperature (up to 1000 K) for the α-Fe_2O_3 nanoparticles. The mean diameter of the nanoparticles is about 60 nm, as determined from the width of the XRD (104) peak (see Fig. 9b). Upon heating the magnetization shows a rapid rise above 650 K, which is the onset temperature of the reduction of the weak ferromagnetic α-Fe_2O_3 to the ferrimagnetic Fe_3O_4 phase. Upon cooling, the magnetization data indicate a magnetic transition at about 850 K (see Fig. 9a), which is the same as the Curie temperature of the Fe_3O_4 phase. The XRD spectrum shown in Fig. 9c, which was taken right after the sample was removed from the magnetometer, confirms this. All the peaks can be indexed by the Fe_3O_4 phase except for the peaks indicated by stars, which represent a minor phase of FeO (less than 10%). From the magnetic hysteresis loop at 330 K (Fig. 9d), we obtain the coercive field H_C to be 87 Oe. After correction for about 10% of FeO and the small difference

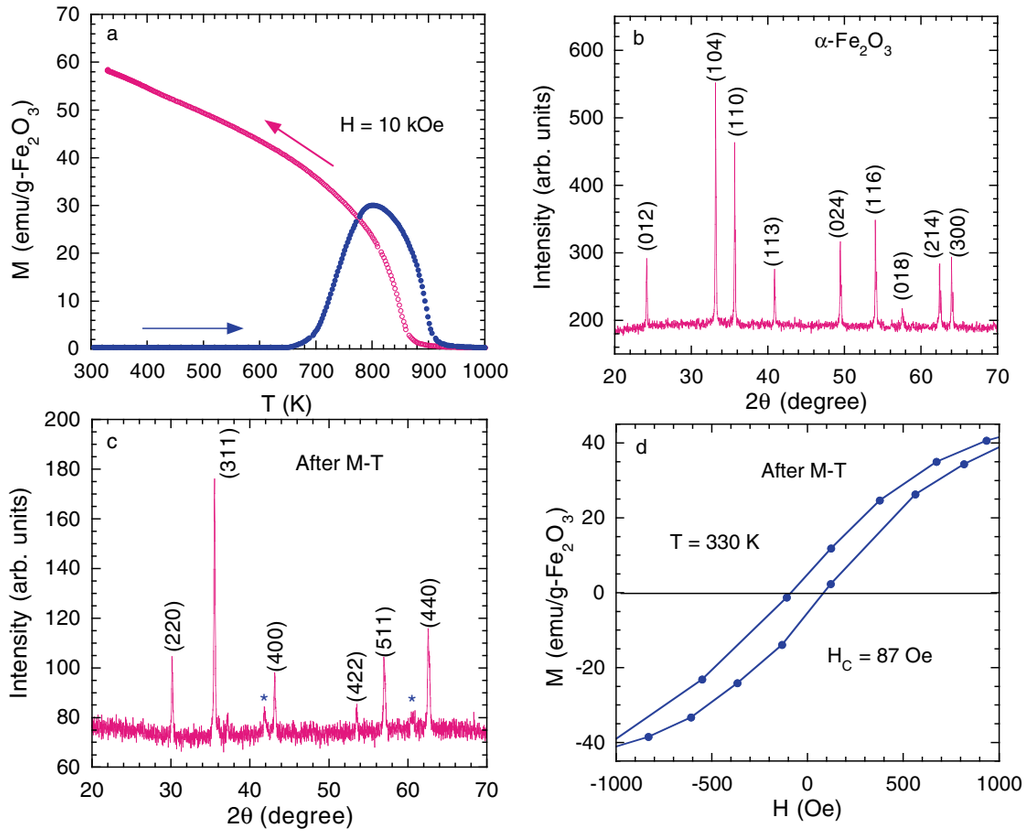

Fig. 9. a) High-field (10 kOe) magnetization versus temperature for α-Fe_2O_3 nanoparticles. b) X-ray diffraction spectrum of the α-Fe_2O_3 nanoparticles. c) XRD spectrum taken right after the sample was removed from the magnetometer. All the peaks can be indexed by the Fe_3O_4 phase except for the peaks indicated by stars, which represent a minor phase of FeO (less than 10%). d) Magnetic hysteresis loop taken at 330 K after the sample was cooled from 1000 K. After Wang et al. (2011).

in the atomic weights of Fe_3O_4 and Fe_2O_3, the saturation magnetization of the converted Fe_3O_4 phase is found to be about 68 emu/g-Fe_3O_4. Since the mean diameter of the converted Fe_3O_4 phase is about 45 nm, as determined from the (311) peak width, the inferred M_s for the 45-nm Fe_3O_4 nanoparticles is in quantitative agreement with the reported value (e.g., M_s = 65 emu/g-Fe_3O_4 and H_C = 156 Oe for d = 55 nm) Goya et al. (2003).

Figure 10a shows temperature dependence of the high-field magnetization for the residual of the mat sample. The magnetization was calculated according to the content of the α-Fe_2O_3 phase in the residual, which was determined by the ICP-MS. For the first run, the sample was heated up to 920 K and measured in a field of 20 kOe. For the second run, it was heated up to 1000 K and measured in a field of 10 kOe. The magnetization data suggest that the α-Fe_2O_3 phase in the residual was not completely reduced to the Fe_3O_4 phase after the first run possibly because the temperature of 920 K is not high enough. After the second run up to 1000 K, the remaining α-Fe_2O_3 phase should be completely reduced to Fe_3O_4 and the magnetization increases by about 34%. The final saturation magnetization at 320 K is about 67 emu/g-Fe_2O_3 or 69 emu/g-Fe_3O_4, which is about 10% larger than that (60 emu/g-Fe_2O_3) for the 60-nm α-Fe_2O_3 nanoparticles (see Fig. 9). The discrepancy should arise from larger

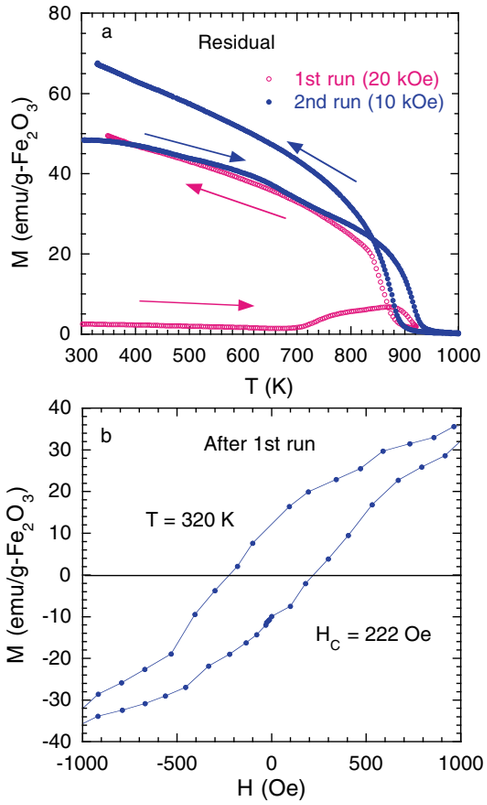

Fig. 10. a) High-field magnetization versus temperature for the residual of the mat sample. In the first run, the applied magnetic field is 20 kOe while in the second run the field is 10 kOe. b) Magnetic hysteresis loop taken at 320 K after the sample was cooled from 920 K in the first run.

particle sizes and higher coercive field of the converted Fe_3O_4 nanoparticles in the residual. The magnetic hysteresis loop shown in Fig. 10b yields H_C = 222 Oe, which is a factor of 2.5 larger than that for the 45-nm Fe_3O_4. By comparing the measured H_C = 222 Oe for the residual with the size dependence of H_C for Fe_3O_4 nanoparticles Goya et al. (2003), we estimate d = 100 nm and M_s = 70 emu/g-Fe_3O_4 for the converted Fe_3O_4 nanoparticles in the residual. Therefore, the magnetization data of the residual are in quantitative agreement with the Fe concentration determined by the ICP-MS.

Figure 11 shows zero-field-cooled (ZFC) and field-cooled (FC) susceptibility for sample RS0657. The sample was first heated up to 1000 K and cooled down to 320 K in a "zero" field. A magnetic field of 2.0 Oe was applied at 320 K and the ZFC susceptibility was measured upon warming up to 1000 K. The FC susceptibility was taken when the temperature is lowered from 1000 K to 320 K. The FC and ZFC susceptibilities clearly show a large thermal hysteresis up to the Curie temperature of about 850 K, which should be associated with the ferrimagnetic transition of the Fe_3O_4 impurity phase. Our previous data Zhao et al. (2008) showed a similar magnetic transition, but the transition temperature was around 1000 K, about 18% higher than that reported here. We have found that the systematically higher Curie temperatures reported in Zhao et al. (2008) arise from an undesirable thermal contact between the sample and the radiation shield (copper foil) of the heat stick. The current ZFC and FC susceptibility data were obtained when the sample was thermally insulated from the radiation shield. Incomplete

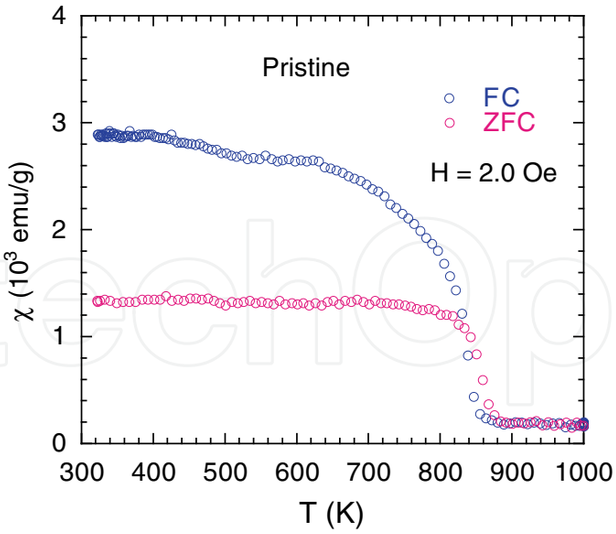

Fig. 11. Temperature dependencies of the zero-field-cooled (ZFC) and field-cooled (FC) susceptibility for a mat sample of RS0657.

thermal insulation always causes a thermal gradient between the sample and thermometer and special attention to this problem must be paid for sample mounting. Fortunately, this thermal gradient is found to be linearly proportional to $T-300$ K and can be corrected easily.

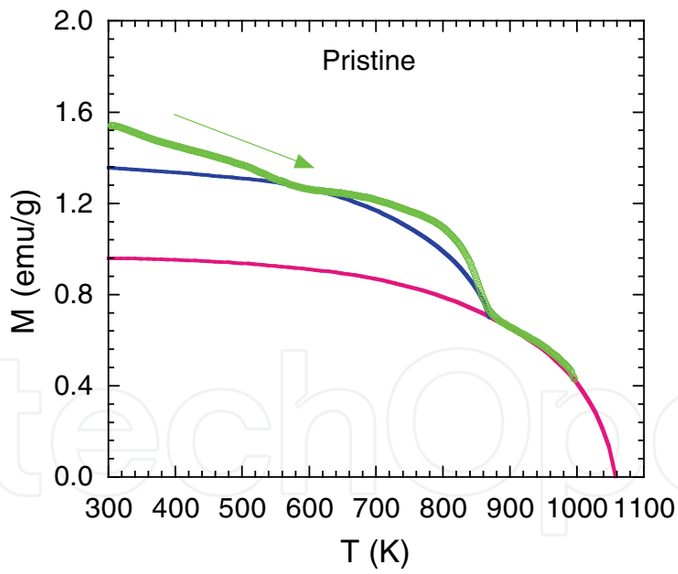

Fig. 12. Temperature dependence of the high-field (20 kOe) magnetization for a virgin sample of RS0657. The data are reproduced from Zhao et al. (2008) and the temperatures are corrected by matching the Curie temperature of the Fe_3O_4 impurity phase. The solid red line is a simulated curve for the Fe impurity phase with $M_s(300K)$ = 0.96 emu/g and T_C = 1056 K and the solid blue line fit is a simulated curve for the Fe_3O_4 impurity phase with $M_s(300K)$ = 0.40 emu/g and T_C = 870 K.

Figure 12 shows temperature dependence of the magnetization for a pristine sample of RS0657, which was measured upon heating in a magnetic field of 20 kOe. The data are

reproduced from Zhao et al. (2008) and the temperatures are corrected by matching the Curie temperature of the Fe_3O_4 impurity phase. Since the magnetization in 20 kOe is close to the saturation magnetization Zhao et al. (2008), the temperature dependence of the saturation magnetization is approximated by the temperature dependence of the magnetization in 20 kOe. It is clear that there are two major magnetic transitions associated with the ferrimagnetic Fe_3O_4 impurity phase and the ferromagnetic α-Fe impurity phase. We can identify the magnetic contributions of the Fe and Fe_3O_4 impurity phases by simulation of their magnetizations with the measured curve of $M_s(T)/M_s(0)$ versus T/T_C for ferromagnetic nickel. The solid red line is a simulated curve for the Fe impurity phase with $M_s(300K)$ = 0.96 emu/g and T_C = 1056 K and the solid blue line is a simulated curve for the Fe_3O_4 impurity phase with $M_s(300K)$ = 0.40 emu/g and T_C = 870 K. There is a significant difference between the data and simulated curve for Fe_3O_4 at temperatures above 640 K. This is caused by the reduction of the α-Fe_2O_3 phase to the Fe_3O_4 phase, as seen in Fig. 9. The remaining $M_s(300K)$ = 0.18 emu/g should contribute from the Fe_3C impurity phase with a Curie temperature of about 476 K, which is clearly seen in the FC susceptibility shown in Fig. 11.

With $M_s(300K)$ = 0.96 emu/g for the α-Fe phase with the concentration of 0.24% and mean diameter of 46 nm, we calculate the saturation magnetization to be 400 emu per gram of Fe. For free Fe nanoparticles with a mean diameter of 46 nm, the saturation magnetization can be extrapolated to be 160 emu per gram of Fe from the measured diameter dependence of $M_s(300K)$ Gong et al. (1991). It is apparent that the saturation magnetization of the 46-nm Fe nanoparticles embedded in MWCNTs is enhanced by a factor of about 2.5 compared with that of free Fe nanoparticles.

With $M_s(300K)$ = 0.40 emu/g for the Fe_3O_4 phase with the concentration of 0.25% and mean diameter of 18 nm, we calculate the saturation magnetization to be 160 emu per gram of Fe_3O_4. For free Fe_3O_4 nanoparticles with a mean diameter of 18 nm, the $M_s(300K)$ value can be inferred to be about 62 emu per gram of Fe_3O_4 from the measured diameter dependence of $M_s(300K)$ Goya et al. (2003). Then, the $M_s(300K)$ value of the 18-nm Fe nanoparticles embedded in MWCNTs is enhanced by a factor of about 2.6 compared with that of free Fe_3O_4 nanoparticles. This enhancement is almost the same as that for the 46-nm Fe nanoparticles embedded in MWCNTs within the experimental uncertainty.

For the Fe_3C impurity phase, the impurity concentration is 0.11$\pm$0.04% and $M_s(300K)$ = 0.18 emu/g, so the saturation magnetization is calculated to be 165$\pm$75 emu per gram of Fe_3C. The enhancement factor is difficult to estimate because the mean diameter of the Fe_3C nanoparticles is unknown and the concentration has a large uncertainty.

The moment enhancement factor of Fe_3O_4 nanoparticles can be also determined independently from the magnetization data of an annealed sample of RS0657. After annealing a pristine sample of RS0657 in air at 480 °C for about 5 minutes, most Fe and Fe_3O_4 nanoparticles have been oxidized into α-Fe_2O_3, as clearly demonstrated from Fig. 13a. The magnetic hysteresis loop at 305 K shows a saturation magnetization of 0.25 emu/g, which is dramatically reduced compared with that (1.54 emu/g) of the pristine sample. Fig. 13b shows the temperature dependence of the high-field magnetization for the annealed sample. After the sample was heated to 990 K, the α-Fe_2O_3 phase in the annealed sample was converted to the Fe_3O_4 phase, similar to the results shown in Figs. 9 and 10. At 980 K, the saturation magnetization is about 0.06 emu/g, which is reduced by a factor of about 8 compared with that of the pristine sample. This implies that only about 0.03% Fe impurity phase is left in the annealed sample. Therefore, after the annealed sample was cooled to 320 K, the total Fe_3O_4 concentration should be 0.91%. This implies that the room-temperature saturation magnetization of the converted Fe_3O_4 is 180 emu per gram of Fe_3O_4. Since the H_C value

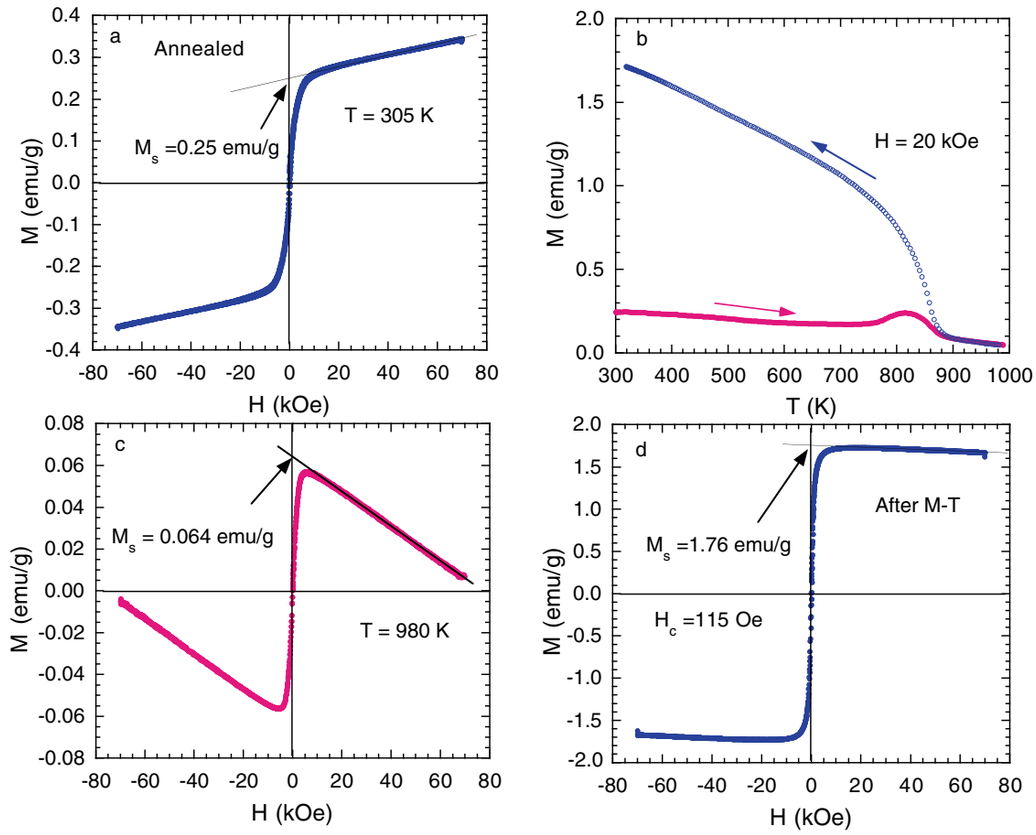

Fig. 13. a) Magnetic hysteresis loop at 305 K for an annealed sample of RS0657. b) Temperature dependence of the high-field (20 kOe) magnetization for the annealed sample. c) Magnetic hysteresis loop at 980 K for the annealed sample. d) Magnetic hysteresis loop taken at 320 K after the sample was cooled from 990 K.

of the converted Fe_3O_4 is 115 Oe, similar to that of the 55 nm Fe_3O_4 nanoparticles Goya et al. (2003), the $M_s(300K)$ value for the converted Fe_3O_4 nanoparticles would be about 65 emu per gram of Fe_3O_4 if they would be isolated from MWCNTs. This implies that the moment enhancement factor is 2.8, very close to the value deduced above.

Above results clearly demonstrate that the moment enhancement factor is nearly independent of the particle size. Furthermore, the moment enhancement factors for Ni, Fe, and Fe_3O_4 nanoparticles are all close to 3, independent of the mean particle diameters that are varied from 11 nm to 46 nm.

5. Plausible interpretations of the giant moment enhancements

We have precisely determined the magnetic impurity concentrations from the high-energy x-ray diffraction spectra, which are all in quantitative agreement with those determined independently from ICP-MS. These analyses along with the magnetic data allow us to precisely determine the saturation magnetizations for various magnetic nanoparticles embedded in MWCNTs. It turns out that the saturation magnetizations for all the nanoparticles embedded in MWCNTs are greatly enhanced compared with those of free (unembedded) nanoparticles. For 10-nm Fe_3C, the saturation magnetization M_s is 156 emu/g-Fe_3C, which is enhanced by ΔM_s = 60 emu/g-Fe_3C or 473 emu/cc-Fe_3C, compared

with the value (93 emu/g) for free particles. Similarly, from the measured results above, we find that ΔM_s = 653 emu/cc-Ni for 11-nm Ni nanoparticles, ΔM_s = 1891 emu/cc-Fe for 46-nm Fe nanoparticles, and ΔM_s = 506 emu/cc-Fe_3O_4 for 18-nm Fe_3O_4 nanoparticles, and 595 emu/cc-Fe_3O_4 for 55-nm Fe_3O_4 nanoparticles.

Now we turn to discuss the origin of the giant magnetization enhancement of the magnetic nanoparticles embedded in MWCNTs. One possibility is that this enhancement arises from a large magnetic proximity effect Cespedes et al. (2004); Coey et al. (2002). We consider a simple case where our ferromagnetic nanoparticles have a cylindrical shape with both length and diameter equal to d and the curved surface of the cylinder contacts with the innermost shell of a MWCNT (this is the most favorable case for the proximity effect). The curved surface area is equal to πd^2 and the total number of the contact carbon is $\pi N_c d^2$, where N_c is the number of carbon per unit area and equal to $3.82\times10^{15}/\text{cm}^2$ Wallace (1947). If the induced magnetic moment is $m\mu_B$ per contact carbon atom, then the induced saturation magnetization normalized to the volume of the ferromagnetic nanoparticle is $\Delta M_s = 4N_c m\mu_B/d = 1420(m/d)$ emu/cc (here d is in units of nm). Using the measured ΔM_s = 653 emu/cc and d = 11 nm for ferromagnetic nickel nanoparticles, we find that m = 5.1, which is a factor of 51 larger than the value ($\sim$0.1) calculated using density function theory Cespedes et al. (2004). For ferromagnetic iron nanoparticles with d = 46 nm, the measured ΔM_s = 1891 emu/cc. This implies m = 61, which is about three orders of magnitude larger than the value predicted from the magnetic proximity effect. For Fe_3C, ΔM_s = 473 emu/cc and d = 10 nm, we find m = 3.3. For Fe_3O_4 with ΔM_s = 506 emu/cc and d = 18 nm, we calculate m = 6.4. For Fe_3O_4 with ΔM_s = 595 emu/cc and d = 55 nm, we calculate m = 23. For the same type (Fe_3O_4) of magnetic nanoparticles and the same MWCNTs, it is hard to imagine the enhanced moment per carbon atom would be so different within the magnetic proximity effect. Further, the magnetic proximity model also predicts two distinctive magnetic transitions Coey et al. (2002), which are not seen in our magnetic data. Therefore, the magnetic proximity model is unlikely to explain our magnetic data.

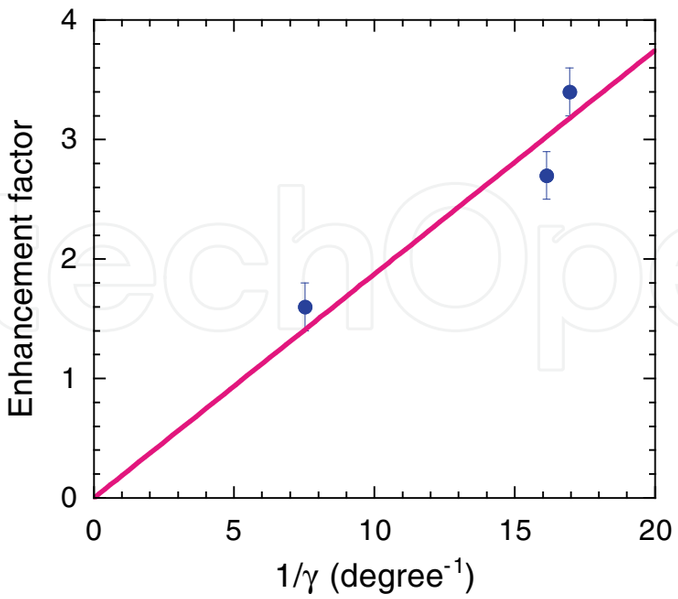

Fig. 14. The moment enhancement factor as a function of the reciprocal of the full width at half maximum of the Gaussian function, fitted for the MWCNT (002) peak.

Alternatively, it is possible that a strong diamagnetic tube could enhance the extrinsic magnetic moment of a (single-domain) magnet embedded inside it. If the tube were a perfect diamagnet, the "poles" of the magnet would be extended further apart (to the length of the tube) without changing their strength, thus giving an extrinsic enhancement to the magnetic moment. This is because the perfect diamagnetism of the tube prevents the magnetic field lines of the magnet from leaking out through the wall of the tube. With this picture, one should expect that the moment enhancement factor should increase with increasing the diamagnetism for the magnetic field parallel to the tube axes. This scenario can naturally explain why the enhancement factors are similar in samples TS0636 and RS0657 with similar numbers of shells while a smaller enhancement factor is found for sample PD15L520 with a much smaller number of shells. In fact, the enhancement factor is inversely proportional to the width of the Gaussian function, fitted for the (002) peak of MWCNTs, as shown in Fig. 14. Since the wall thickness is inversely proportional to the width, the enhancement factor is simply proportional to the thickness of the nanotube wall.

The plausibility of this interpretation depends on whether MWCNTs show strong diamagnetism when the magnetic field is applied in the tube-axis direction in which the orbital diamagnetism is negligibly small Lu (1995). If MWCNTs are ultrahigh temperature superconductors, they will exhibit strong diamagnetism. The observation of superconducting-like hysteresis loops in HOPG at 400 K should be a good indication of local superconductivity well above room temperature Kopelevich et al. (2000). Similarly, there is also compelling evidence for ultrahigh temperature superconductivity in MWCNTs [see a review article Zhao (2004)]. A recent theoretical work Black-Schaffer & Doniach (2007) predicts ultrahigh temperature d-wave superconductivity in well-doped graphene based on RVB theory originally proposed by Anderson Anderson (1987). A similar model for layered cuprates Lee et al. (2006) predicts that an optimal superconducting transition temperature $T_c \simeq 0.14J/k_B$ (where J is the antiferromagnetic exchange energy and k_B is the Boltzmann constant). In graphene, $J \simeq t \simeq 3.0$ eV Black-Schaffer & Doniach (2007), so the optimal T_c should be about 0.42 eV$/k_B \simeq 5000$ K, in quantitative agreement with the numerical calculation Black-Schaffer & Doniach (2007). Very recent large-scale quantum Monte Carlo simulations of correlated Dirac fermions on a honeycomb lattice (realized in graphene) have confirmed the existence of a short-range RVB liquid Meng et al. (2010). If the RVB theory for superconductivity is relevant, ultrahigh temperature superconductivity can be realized in the MWCNTs where sufficient doping is realized by charge-transfer between ferromagnetic nanoparticles and MWCNTs. The special morphology (granular nature) in the mat samples, and the presence of magnetic nanoparticles can also promote the paramagnetic Meissner effect, which could also explain our magnetic data.

6. Identification of the diamagnetic Meissner effect in pure MWCNTs

One of the most important signatures of superconductivity is the existence of the diamagnetic Meissner effect. Therefore, it is essential to provide evidence for the existence of the diamagnetic Meissner effect to prove ultrahigh temperature superconductivity. However, the diamagnetic Meissner effect may be less visible because the outer diameters of the tubes may be much smaller than the magnetic penetration depth. Further, the orbital diamagnetic susceptibility in the magnetic field perpendicular to the graphite sheet is large, making it difficult to separate the diamagnetic Meissner effect from the large orbital diamagnetic susceptibility. Fortunately, the orbital diamagnetic susceptibility of carbon nanotubes in the magnetic field parallel to the tube axes is predicted to be very small at room temperature Lu

(1995). This makes it possible to extract the diamagnetic Meissner effect from the measured susceptibility in the parallel field.

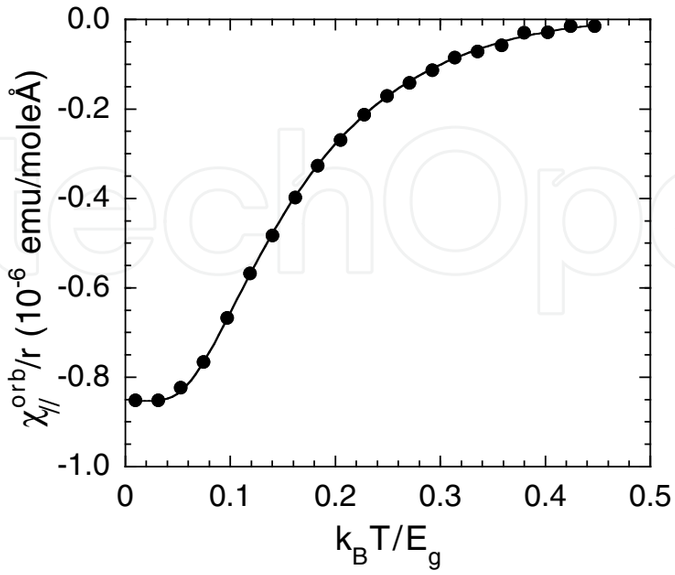

Fig. 15. The calculated temperature dependence of the orbital diamagnetic susceptibility of a single-walled carbon nanotube in the parallel magnetic field. The calculation is based on the tight-binding approximation Lu (1995).

Figure 15 shows the temperature dependence of the orbital diamagnetic susceptibility of a single-walled carbon nanotube in the parallel magnetic field (solid circles), which was calculated based on the tight-binding approximation Lu (1995). Here $E_g = \gamma_\circ a_{C-C}/r$, a_{C-C} (= 0.142 nm) is the bonding length, r is the radius of the tube, and $\gamma_\circ$ (= 2.6 eV) is the tight-binding transfer matrix element Lu (1995). What is remarkable is that the temperature dependence of the orbital susceptibility can be perfectly fitted by an equation (solid line):

$$\frac{\chi_{\parallel}^{orb}(T)}{r} = \frac{\chi_{\parallel}^{orb}(0)}{r}[1 - 1.242\sqrt{E_g/k_BT}\exp(-0.283E_g/k_BT)]. \quad (1)$$

From Eq. 1, we can determine the orbital diamagnetic contribution for a tube or shell. To calculate the orbital diamagnetic susceptibility for a multi-walled carbon nanotube comprising several concentric shells, one needs to replace E_g and r in Eq. 1 by the averaged $< E_g >$ and $< r >$. Since both $\chi_{\parallel}^{orb}$ and the mass of each shell are proportional to r, the average $< r >$ should be $(2/3)r_{out}$ (where r_{out} is the outer radius of a MWCNT). Considering the fact that $\chi_{\parallel}^{orb}$ is proportional to $\gamma_\circ^2$ Kotosonov & Kuvshinnikov (1997), we finally have

$$\chi_{\parallel}^{orb}(T) = -7.0 \times 10^{-9}\gamma_\circ^2 r_{out}[1 - 1.52\sqrt{\frac{a_{C-C}\gamma_\circ}{r_{out}k_BT}}\exp(-\frac{0.425a_{C-C}\gamma_\circ}{r_{out}k_BT})], \quad (2)$$

where $\chi_{\parallel}^{orb}$, $\gamma_\circ$, and r_{out} are in units of emu/g, eV, and Å, respectively.

Now we consider the diamagnetic Meissner effect for a superconducting MWCNT in the magnetic field parallel to the tube axis. We are particularly interested in the case where the magnetic penetration depth is larger than the outer radius of the tube. In this case, the

diamagnetic susceptibility due to the Meissner effect is given by

$$\chi_{\parallel}^{S}(T) = -\frac{r_{out}^2}{32\pi\lambda_{\theta}^2(T)}, \tag{3}$$

where $\lambda_{\theta}(T)$ is the penetration depth when carriers move along the circumferential direction (or the field is parallel to the tube axis). For a macroscopic sample consisting of a macroscopic number of MWCNTs, the r_{out}^2 in the above equation should be replaced by $< r_{out}^2 >$, the average of r_{out}^2. In the low temperature limit: $k_B T \leq 0.2\Delta_{min}(0)$ [where $\Delta_{min}(0)$ is the minimum value of the superconducting gap at zero temperature], the penetration depth follows the following expression:

$$\lambda_{\theta}(T) = \lambda_{\theta}(0) + \lambda_{\theta}(0)\sqrt{\pi\Delta_{min}(0)/2k_B T}\exp[-\Delta_{min}(0)/k_B T]. \tag{4}$$

Combining Eqs. 3 and 4, we can readily show that

$$\chi_{\parallel}^{S}(T) = \chi_{\parallel}^{S}(0)(1 - 2\sqrt{\pi\Delta_{min}(0)/2k_B T}\exp[-\Delta_{min}(0)/k_B T]). \tag{5}$$

The total diamagnetic contribution of a superconducting MWCNT is the sum of $\chi_{\parallel}^{S}(T)$ and $\chi_{\parallel}^{orb}(T)$, that is,

$$\begin{aligned}\chi_{\parallel}(T) = {} & \chi_{\parallel}^{S}(0)(1 - 2\sqrt{\pi\Delta_{min}(0)/2k_B T}\exp[-\Delta_{min}(0)/k_B T]) \\ & -7.0\times 10^{-9}\gamma_{\circ}^2 r_{out}[1 - 1.52\sqrt{\frac{a_{C-C}\gamma_{\circ}}{r_{out}k_B T}}\exp(-\frac{0.425 a_{C-C}\gamma_{\circ}}{r_{out}k_B T})].\end{aligned} \tag{6}$$

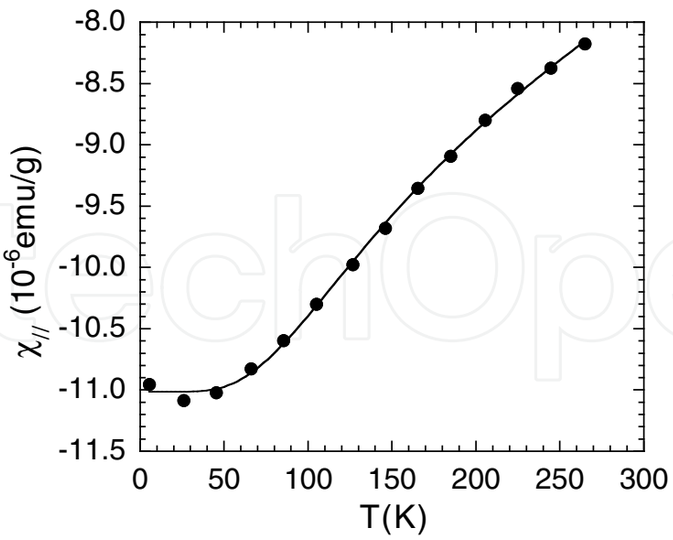

Fig. 16. Temperature dependence of the susceptibility for physically separated and aligned MWCNTs in a magnetic field parallel to the tube axes. The data are extracted from Chauvet et al. (1995).

Figure 16 shows the temperature dependence of the parallel-field susceptibility for pure MWCNTs, which are physically separated and aligned Chauvet et al. (1995). The outer diameters of the tubes are 10±5 nm and the lengths are on the order of 1 μm Chauvet et al. (1995). It is apparent that the diamagnetic susceptibility is significant up to 265 K. If these MWCNTs are ultrahigh-temperature superconductors with $\Delta_{min} \geq 100$ meV, the data should be consistent with Eq. 6. The solid line in Fig. 16 is the best fitted curve by Eq. 6. It is striking that the fit is excellent. The fitting parameters are the following: $\chi_{\parallel}^{S}(0) = -(7.6\pm0.2)\times10^{-6}$ emu/g, Δ_{min} = 124±14 meV, $\gamma_\circ$ = 2.80±0.09 eV, and r_{out} = 62.9±0.7 Å. The value of Δ_{min} = 124 meV justifies the temperature range for the fitting. If we use the BCS relation between the gap and superconducting transition temperature: $T_c = \Delta(0)/1.76k_B$, we find that $T_c \geq 800$ K. The value of r_{out} = 62.9 Å is consistent with the average outer radius of 50±25 Å, which was directly measured by TEM Chauvet et al. (1995). The value of $\gamma_\circ$ = 2.80 eV is in quantitative agreement with both theory and experiment.

Now we would like to check if the fitted parameter $\chi_{\parallel}^{S}(0) = -(7.6\pm0.2)\times10^{-6}$ emu/g is consistent with the expected Meissner effect. If we assume that the outer radii of MWCNTs are equally distributed from 23 to 103 Å with $< r_{out} >$ = 63 Å (in agreement with that inferred from the best fit above), we find $< r_{out}^2 >$ = 4502 Å^2. With the weight density of 2.17 g/cm^3 Qian et al. (2000) and $\chi_{\parallel}^{S}(0) = -7.6\times10^{-6}$ emu/g, we calculate $\lambda_\theta(0) \simeq 1648$ Å using Eq. 3. This value of the penetration depth corresponds to $n/m_\theta^* = 1.04\times10^{21}/\mathrm{cm}^3 m_e$, where n is the carrier density, m_θ^* is the effective mass of carriers along the circumferential direction. If we take $m_\theta^* = 0.012 m_e$, typical for graphite Bayot et al. (1989), we estimate $n = 1.25\times10^{19}/\mathrm{cm}^3$, in quantitative agreement with the Hall effect measurement Baumgartner et al. (1997) which gives $n = 1.6\times10^{19}/\mathrm{cm}^3$. It is worthy of noting that the inferred magnetic penetration depth is far larger than the outer radii of MWCNTs, which justifies Eq. 3. This also ensures that the Hall effect in the superconducting state is the same as that in the normal state.

A carbon nanotube should behave like graphene when the electron mean free path is shorter than the circumference of the tube Schönenberger et al. (1999). In graphene, the effective mass of carriers is given by $m^* = \sqrt{\pi n_{2D}}\hbar/v_F$ Novoselov et al. (2005), where n_{2D} is the sheet carrier density and v_F is the Fermi velocity. Using $\hbar v_F = 1.5 a_{C-C}\gamma_\circ$ = 5.96 eVÅ and taking n = 1.6× $10^{19}/\mathrm{cm}^3$, we find that m^* = 0.018 m_e. This leads to $n/m^* = 0.89\times10^{21}/\mathrm{cm}^3 m_e$, very close to what we have inferred from the susceptibility data. Therefore, the susceptibility data of the aligned MWCNTs are in quantitative agreement with ultrahigh temperature superconductivity.

7. Concluding remarks

It is well known that copper-based perovskite oxides rightly enjoy consensus as high-temperature superconductors on the basis of two signatures: the resistive transition and the Meissner effect. Here we have provided magnetic evidence for ultrahigh temperature superconductivity in carbon nanotubes. The giant magnetic moment enhancement found for the magnetic nanoparticles embedded in MWCNTs cannot be explained by the magnetic proximity effect. But rather the result can be naturally explained in terms of the interplay between magnetism of the magnetic nanoparticles and ultrahigh temperature superconductivity in multi-walled carbon nanotubes. The diamagnetic susceptibility of pure MWCNTs for the field parallel to the tube axes agrees quantitatively with the predicted penetration depth from the measured carrier density. Furthermore, bundling of individual MWCNTs into closely packed bundles leads to a large enhancement in the

diamagnetic susceptibility, which can be naturally explained by the Josephson coupling among the tubes in the bundles Zhao et al. (2008). Because of a finite number of transverse conduction channels, both quantum and thermally activated phase slips are important and the on-tube resistance will never go to zero below the mean-field superconducting transition temperature. Nonetheless, the room-temperature on-tube resistance has been found to be indistinguishable from zero for many individual MWCNTs De Pablo et al. (1999); Frank et al. (1998); Poncharal et al. (2002); Urbina et al. (2003).

There are also other independent evidences for ultrahigh temperature superconductivity in both SWCNTs and MWCNTs Zhao & Wang (2001); Zhao (2004; 2006). Some resistivity data of MWCNTs and SWCNTs show quite broad superconducting transitions above room temperature and can be well explained Zhao (2006) in terms of thermally activated phase slip theory developed by Langer, Ambegaokar, McCumber, and Halperin. Raman data and tunneling spectra of SWCNTs consistently show single particle excitation gaps in the range of 100-200 meV Zhao (2006). This would imply that T_{c0} = 600-1200 K. The tunneling spectra of some MWCNTs also indicate a gap of about 200 meV, which is too large to be consistent with the expected semiconducting gap for semiconducting-chirality tubes Zhao (2006).

Although electron-phonon coupling in graphite and related materials is strong and the phonon energy is high ($>$ 100 meV), the calculated electron-phonon coupling constants for various carbon-based materials Barnett et al. (2005); Park et al. (2008) are small due to low density of states. This implies that electron-phonon interaction alone would be insufficient to explain ultrahigh temperature superconductivity in carbon nanotubes, graphite, and carbon films. Although the RVB theory Anderson (1987); Black-Schaffer & Doniach (2007) might be able to explain ultrahigh temperature superconductivity in heavily-doped graphene and MWCNTs, it does not predict ultrahigh temperature superconductivity at low doping. We speculate that strong electron-electron correlation of the relativistic Dirac fermions may lead to a huge enhancement of electron-phonon coupling. Indeed, the electron-phonon coupling constant has been calculated to be about 0.04 for graphene and graphite Park et al. (2008) while the coupling constant determined by angle-resolved photoemission spectroscopy is about 1.0 Sugawara et al. (2007). The enhancement factor is over one order of magnitude, similar to the case in strongly correlated cuprates. The strongly enhanced electron-phonon coupling along with strong coupling to the high-energy acoustic plasmons inherent in quasi-1D and 2D electronic systems Cui & Tsai (1991); Lee & Mendoza (1989) may be the key to achieve ultrahigh temperature superconductivity. In order to take further advantage of strong electron-electron correlation, the order parameters in doubly-degenerate bands near K and K' points might be of opposite signs (nodelss d-wave). Another important factor to influence superconductivity in carbon nanotubes is the strong long-range Coulomb interaction, which can completely destroy superconductivity if it is not well screened by substrates and/or electrodes De Martino & Egger (2004); Zhao (2006). More extensive experimental and theoretical investigations are required to understand the pairing mechanism of ultrahigh temperature superconductivity in carbon-related materials.

Acknowledgment: We thank M. Du and F. M. Zhou for the elemental analyses using ICP-MS. Use of the Advanced Photon Source was supported by the U.S. Department of Energy, Office of Science, Office of Basic Energy Sciences, under Contract No. DE-AC02-06CH11357. This work was partly supported by the National Natural Science Foundation of China (10874095) and Y. G. Bao's Foundation.

8. References

Alexandrov, A. S. & Mott, N. F. (1995). *Polarons and Bipolarons*, World Scientific, ISBN-981022298X, Singapore.

Anderson, P. W. (1987). The Resonating Valence Bond State in La_2CuO_4 and Superconductivity. *Science*, 235, 4793, (March 1987) 1196-1198.

Antonowicz, K. (1974). Possible superconductivity at room temperature. *Nature (London)*, 247, 5440, (February 1974) 358-360.

Barnett, R.; Demler, E. & Kaxiras, E. (2005). Electron-phonon interaction in ultrasmall-radius carbon nanotubes. *Phys. Rev. B*, 71, 3, (January 2005) 035429-035450.

Baskaran, G. & Jafari, S. A. (2002). Gapless Spin-1 Neutral Collective Mode Branch for Graphite. *Phys. Rev. Lett.* 89, 1, (June 2002) 016402-016405.

Baumgartner, G.; Carrard, M.; Zuppiroli, L.; Bacsa, W.; De Heer, W. A. & Forro, L. (1997). Hall effect and magnetoresistance of carbon nanotube films. *Phys. Rev. B*, 55, 11, (March 1997) 6704-6707.

Bayot, V.; Piraux, L.; Michenaud, J.-P. & Issi, J. -P. (1989). Weak localization in pregraphitic carbon fibers. *Phys. Rev. B*, 40, 6, (August 1989) 3514-3523.

Black-Schaffer, A. M. & Doniach, S. (2007). Resonating valence bonds and mean-field d-wave superconductivity in graphite. *Phys. Rev. B*, 75, 13, (April 2007) 134512-134521.

Chauvet, O; Forro, L.; Bacsa, W.; Ugarte, D.; Doudin, B. & de Heer, W. A. (1995). Magnetic anisotropies of aligned carbon nanotubes. *Phys. Rev. B*, 52, 10, (September 1995) R6963-6966.

Chen, D. H.& Hsieh, C. H. (2002). Synthesis of nickel nanoparticles in aqueous cationic surfactant solutions. *J. Mater. Chem.*, 12, 8, (June 2002) 2412-2415.

Cervenka, J.; Katsnelson, M. I. & Flipse, C. F. J. (2009). Room-temperature ferromagnetism in graphite driven by two-dimensional networks of point defects. *Nature Physics*, 5, 11, (October 2009) 840-844.

Cespedes, O.; Ferreira, M. S.; Sanvito, S.; Kociak, M. & Coey, J. M. D. (2004). Contact induced magnetism in carbon nanotubes. *J. Phys.: Condens. Matter*, 16, 10, (February 2004) L155-162.

Coey, J. M. D.; Venkatesan, M.; Fitzgerald, C. B.; Douvalis, A. P.& Sanders, I. S. (2002). Ferromagnetism of a graphite nodule from the Canyon Diablo meteorite. *Nature (London)*, 420, 6912, (November 2002) 156-159.

Cui, S. M. & Tsai, C. H. (1991). Plasmon theory of high-Tc superconductivity. *Phys. Rev. B*, 44, 22, (December 1991) 12500-12510.

Da Silva, R. R.; Torres, J. H. S. & Kopelevich, Y. (2001). Indication of Superconductivity at 35 K in Graphite-Sulfur Composites. *Phys. Rev. Lett.* 87, 14, (September 2001) 147001-147003.

De Martino, A. & Egger, R. (2004). Effective low-energy theory of superconductivity in carbon nanotube ropes. *Phys. Rev. B* 70, 1, (July 2004) 014508-014517.

De Pablo, P. J.; Graugnard, E.; Walsh, B.; Andres, R. P.; Datta, S. & Reifenbergera, R. (1999). A simple, reliable technique for making electrical contact to multiwalled carbon nanotubes. *Appl. Phys. Lett.*, 74, 2, (January 1999) 323-325.

Esquinazi, P.; Spemann, D.; Hohne, R.; Setzer, A.; Han, K. H. & Butz, T. (2003). Induced Magnetic Ordering by Proton Irradiation in Graphite. *Phys. Rev. Lett.*, 91, 22, (November 2003) 227201-227204.

Frank, S.; Poncharal, P.; Wang, Z. L.& de Heer, W. A. (1998). Carbon Nanotube Quantum Resistors. *Science*, 280, 5370 (June 1998) 1744-1746.

Ginzburg, V. L. (1982). *High-Temperature Superconductivity*, Plenum Publishing Corporation, ISBN-0306109700, New York.

Gonzalez, J.; Guinea, F. & Vozmediano, M. A. H. (2001). Electron-electron interactions in graphene sheets. *Phys. Rev. B*, 63, 13, (March 2001) 134421-134428.

Gong, W.; Li, H.; Zhao, Z. & Chen, J. (1991). Ultrafine particles of Fe, Co, and Ni ferromagnetic metals. *J. Appl. Phys.*, 69, 8, (April 1991) 5119-5121.

Goya, G. F.; Berquo, T. S.; Fonseca, F. C. & Morales, M. P. (2003). Static and dynamic magnetic properties of spherical magnetite nanoparticles. *J. Appl. Phys.*, 94, 5, (September 2003) 3520-3528.

Kopelevich, Y.; Esquinazi, P.; Torres, J. H. S. & Moehlecke, S. (2000). Ferromagnetic- and Superconducting-Like Behavior of Graphite. *J. Low Temp. Phys.*, 119, 5, (April 2000) 691-702.

Kotosonov, A. S. & Kuvshinnikov, S. V. (1997). Diamagnetism of some quasi-two-dimensional graphites and multiwall carbon nanotubes. *Phys. Lett. A*, 229, 5 (June 1997) 377-380.

Lebedev, S. G. (2004). Particle irradiation for verification of superconducting-like behavior in carbon arc films. *Nucl. Instr. Meth.*, A521, 1, (March 2004) 22-29.

Lee, P. A.; Nagaosa, N. & Wen, X.-G. (2006). Doping a Mott insulator: Physics of high-temperature superconductivity *Rev. Mod. Phys.*, 78, 1, (January 2006) 17-85.

Lee, Y. C. & Mendoza, B. S. (1989). Possible high-Tc superconductivity in thin wires. *Phys. Rev. B*, 39, 7, (March 1989) 4776-4779.

Little, W. A. (1964). *Phys. Rev.*, 164, 6A, (June 1964) A1416-1424.

Lu, J. P. (1995). Novel Magnetic Properties of Carbon Nanotubes. *Phys. Rev. Lett.*, 74, 7, (February 1995) 1123-1126.

Makarova, T. *et al.* (2001). Magnetic carbon. *Nature (London)*, 413, 6857, (October 2001) 716-718.

Mendoza, D.; Morales, F.; Escudero, R. & Walter, J. (1999). Magnetization studies in quasi two-dimensional palladium nanoparticles encapsulated in a graphite host. *J. Phys.: Condens. Matter*, 11, 28, (July 1999) L317-320.

Meng, Z. Y.; Lang, T. C.; Wessel, S.; Assaad, F. F. & Muramatsu, A. (2010). Quantum spin liquid emerging in two-dimensional correlated Dirac fermions. *Nature (London)*, 464, 7290, (April 2010) 847-851

Moehlecke, S.; Ho, C.; & Maple, M. B. (2002). Coexistence of superconductivity and ferromagnetism in the graphite-sulphur system. *Phil. Mag. B*, 82, 12, (August 2002) 1335-1347.

Moehlecke, S.; Kopelevich, Y. & Maple, M. B. (2004). Interaction between superconducting and ferromagnetic order parameters in graphite-sulfur composites. *Phys. Rev. B*, 69, 13, (April 2004) 134519-134523.

Mombru, A. W.; Pardo, H.; Faccio, R.; de Lima, O. F.; Leite, E. R.; Zanelatto, G.; Lanfredi, A. J. C.; Cardoso, C. A. & Araujo-Moreira, F. M. (2005). Multilevel ferromagnetic behavior of room-temperature bulk magnetic graphite. *Phys. Rev. B*, 71, 10, (March 2005) 100404-100407(R).

Novoselov, K. S.; Geim, A. K.; Morozov, S. V.; Jiang, D.; Katsnelson, M. I.; Grigorieva, I. V.; Dubonos, S. V. & Firsov, A. A. (2005). Two-dimensional gas of massless Dirac fermions in graphene. *Nature (London)*, 438, 7065, (November 2005) 197-200.

Park, C.-H.; Giustino, F.; Cohen, M. L. & Louie, S. G. (2008). Electron-Phonon Interactions in Graphene, Bilayer Graphene, and Graphite. *Nano Lett.*, 8, 12, (November 2008) 4229-4233.

Poncharal, P.; Berger, C.; Yi, Y.; Wang, Z. L. & de Heer, W. A. (2002). Room Temperature Ballistic Conduction in Carbon Nanotubes. *J. Phys. Chem. B*, 106, 47, (November 2002) 12104-12118.

Qian, D.; Dickeya, E. C.; Andrews, R. & Rantell, T. (2000). Load transfer and deformation mechanisms in carbon nanotube-polystyrene composites. *Appl. Phys. Lett.*, 76, 20, (May 2000) 2868-2870.

Reznik, D.; Olk, C. H.; Neumann, D. A. & Copley, J. R. D. (1995). X-ray powder diffraction from carbon nanotubes and nanoparticles. *Phys. Rev. B*, 52, 1, (July 1995) 116-124.

Sajitha, E. P.; Prasad, V.; Subramanyam, S. V.; Mishra, A. K.; Sarkar, S. & Bansal, C. (2007). Size-dependent magnetic properties of iron carbide nanoparticles embedded in a carbon matrix. *J. Phys.: Condens. Matter*, 19, 4, (January 2007) 046214(1-13).

Schönenberger, C.; Bachtold, A.; Strunk, C.; Salvetat, J.-P. & Forro, L. (1999). Interference and Interaction in multi-wall carbon nanotubes. *Appl. Phys. A*, 69, 3, (August 1999) 283-295.

Schrieffer, J. R. (2004). Gauge Theory Pairing and Spin Fluctuations Near the Quantum Critical Point. *Low Temp. Phys.*, 32, 4, (April 2006) 359-362.

Sugawara, K.; Sato, T.; Souma, S.; Takahashi, T. & Suematsu, H. (2007). Anomalous Quasiparticle Lifetime and Strong Electron-Phonon Coupling in Graphite. *Phys. Rev. Lett.*, 98, 3, (January 2007) 036801-036804.

Talyzin, A.; Dzwilewski, A.; Dubrovinsky, L.; Setzer, A. & Esquinazi, P. (2007). Structural and magnetic properties of polymerized C60 with Fe. *Eur. Phys. J. B*, 55, 1, (February 2007) 57-62.

Urbina, A.; Echeverrõa, I.; Perez-Garrido, A.; Dõaz-Sanchez, A. & Abellan, J. (2003). Quantum Conductance Steps in Solutions of Multiwalled Carbon Nanotubes. *Phys. Rev. Lett.*, 90, 10, (March 2003) 106603-106606.

Wallace, P. R. (1947). The Band Theory of Graphite. *Phys. Rev.*, 71, 9, (May 1947) 622-634.

Wang, J.; Beeli, P.; Ren, Y. & Zhao, G. M. (2010). Giant magnetic moment enhancement of nickel nanoparticles embedded in multiwalled carbon nanotubes. *Phys. Rev. B*, 82, 19, (November 2010) 193410-193413.

Wang, J.; Wu, W.; Zhao, F. & Zhao, G. M. (2011). Suppression of the Néel temperature in hydrothermally synthesized α-Fe_2O_3 nanoparticles. *J. Appl. Phys.*, 109, 5, (March 2011) 056101-056103.

Zhao, G. M. & Wang, Y. S. (2001). Possible superconductivity above 400 K in carbon-based multiwall nanotubes. arXiv:cond-mat/0111268v2

Zhao, G. M. (2004). Arguments for quasi-one-dimensional room-temperature superconductivity in carbon nanotubes, In: *Molecular Nanowires and Other Quantum Objects*, Alexandrov, A. S.; Demsar, J. & Yanson, I. K. (Ed.), 95-106, Nato Science Series, Kluwer Academic Publishers, ISBN-978-1-4020-2068-1, Netherlands.

Zhao, G. M. (2006). Compelling Evidence of High-Temperature Superconductivity in Carbon Nanotubes, In: *Trends in Nanotubes Research*, Delores A. Martin, D. A., (Ed.), 39-75, Nova Science Publishers, ISBN-1-59454-791-2, New York.

Zhao, G. M. & Beeli, P. (2008). Observation of an ultrahigh-temperature ferromagnetic-like transition in iron-contaminated multiwalled carbon nanotube mats. *Phys. Rev. B*, 77, 24, (June 2008) 245433-245438.

Zhao, G. M.; Wang, J.; Ren, Y. & Beeli, P. (2011). Anomalous thermal hysteresis in the high-field magnetizations of magnetic nanoparticles embedded in multi-walled carbon nanotubes: Consistent with ultrahigh temperature superconductivity. submitted to Nature.

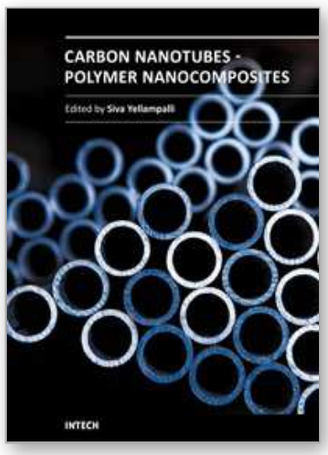

Carbon Nanotubes - Polymer Nanocomposites

Edited by Dr. Siva Yellampalli

ISBN 978-953-307-498-6
Hard cover, 396 pages
Publisher InTech
Published online 17, August, 2011
Published in print edition August, 2011

Polymer nanocomposites are a class of material with a great deal of promise for potential applications in various industries ranging from construction to aerospace. The main difference between polymeric nanocomposites and conventional composites is the filler that is being used for reinforcement. In the nanocomposites the reinforcement is on the order of nanometer that leads to a very different final macroscopic property. Due to this unique feature polymeric nanocomposites have been studied exclusively in the last decade using various nanofillers such as minerals, sheets or fibers. This books focuses on the preparation and property analysis of polymer nanocomposites with CNTs (fibers) as nano fillers. The book has been divided into three sections. The first section deals with fabrication and property analysis of new carbon nanotube structures. The second section deals with preparation and characterization of polymer composites with CNTs followed by the various applications of polymers with CNTs in the third section.

InTech Europe
University Campus STeP Ri
Slavka Krautzeka 83/A
51000 Rijeka, Croatia
Phone: +385 (51) 770 447
Fax: +385 (51) 686 166
www.intechopen.com

InTech China
Unit 405, Office Block, Hotel Equatorial Shanghai
No.65, Yan An Road (West), Shanghai, 200040, China
中国上海市延安西路65号上海国际贵都大饭店办公楼405单元
Phone: +86-21-62489820
Fax: +86-21-62489821

IntechOpen